Res. Educ. Technol. Multicult., 5(3), 293-303, September, 2026

Research in Education, Technology, and Multiculture

ISSN: 3025-6763 | Journal's DOI: 10.61436/rietm

Homepage: https://imrecsjournal.com/journals/index.php/rietm

Hydrodynamic Response Analysis of a Multi-Moonpool Floating Structure Using the Boundary Element Method

Muhammad Taufiq Nur Hidayat[1], Aditya Rio Prabowo[1,*], Ristiyanto Adiputra[1,2], Mahfud Alfajar[3], Oleksiy Melnyk[4], & Martin Jurkovič[5]

[1]Department of Mechanical Engineering, Universitas Sebelas Maret, Indonesia

[2]Research Center for Hydrodynamic Technology, National Research and Innovation Agency, Indonesia

[3]P.T. Internik Nusa Prawira, Indonesia

[4]Department of Navigation and Maritime Safety, Odesa National Maritime University, Ukraine

[5]Faculty of Operation and Economics of Transport and Communication, University of Zilina, Slovakia

ARTICLE INFO

Article History:

Received: 07 July 2026

Accepted: 27 August 2026

Published: 08 September 2026

Keywords:

Boundary element method;

Floating structure;

Hydrodynamics;

Moonpool;

Piston mode resonance.

Corresponding Author:

aditya@ft.uns.ac.id

ABSTRACT

This study aims to evaluate the hydrodynamic response of a displacement-type hull integrated with a multi-moonpool system (one main and sequential cylindrical moonpools) using the Boundary Element Method (BEM), addressing the critical challenge of piston-mode resonance that causes excessive heave motion. The analysis used ANSYS AQWA based on linearized potential-flow theory, assuming infinite water depth and head-sea conditions. Grid independence tests were conducted at resolutions ranging from 5.0 m to 0.7 m, and the resulting Heave RAO curve was benchmarked against a reference dataset. A significant amplitude deviation was found in the high-frequency zone (piston-mode resonance), where the BEM solver overpredicted the heave RAO by 68.77% relative to the reference curve, while both curves showed near-perfect asymptotic alignment in the macro-wave regime. BEM is reliable for predicting motion response in the macro-wave regime, but future hydrodynamic optimization of moonpool structures requires integrating viscous damping modifiers to realistically capture resonance amplitude peaks.

To cite this article:

Hidayat, M. T. N., Prabowo, A. R., Adiputra, R., Alfajar, M., Melnyk, O., & Jurkovič, M. (2026). Hydrodynamic response analysis of a multi-moonpool floating structure using the boundary element method. *Research in Education, Technology, and Multiculture*, *5*(3), 293-303. doi: https://doi.org/10.61436/rietm/v5i3.pp293-303

■ INTRODUCTION

Over the past decade, marine engineering architecture has developed rapidly, particularly in the design of large-scale floating structures for deepwater operations. These massive structures serve as the primary foundation for a wide range of modern offshore operations, from deepwater drilling vessels and wind turbine installations to floating production, storage, and offloading (FPSO) facilities and other advanced platforms (Sheng et al., 2022; Zhai et al., 2025). The greatest challenge in operating in the open-sea environment is constant exposure to dynamic wave loads. Therefore, evaluating seakeeping characteristics, the ability of a structure to respond to wave excitation while maintaining its stability and mechanical integrity, is a fundamental parameter in the hull design cycle (Sulovsky et al., 2023).

Excessive structural motion response due to wave impact can be fatal. Dynamic motion fluctuations and hydroelastic deformations not only disrupt operational efficiency but also risk compromising the integrity of underwater installations (Zhao et al., 2023). In extreme scenarios, excessive pressure can lead to complete failure of the mooring system, directly endangering the entire platform system (Chen et al., 2024). To mitigate this while optimizing underwater accessibility, modern floating platform designs have incorporated moonpool systems (Zou et al., 2024). In essence, a moonpool is a practical vertical opening in a ship's hull that provides direct access to the seabed, which is inherently protected from surface-wave interactions (Guo et al., 2017). Installing this hull gap introduces significant hydrodynamic complexity, despite greatly simplifying operational demands (Cui et al., 2022). The presence of a moonpool changes the fluid flow properties around the hull, increasing hydrodynamic drag (Shahabadi et al., 2017; Hu et al., 2026). Furthermore, the mean wave drift force, an important metric for platform positional stability, is strongly influenced by the complex fluid interactions around the moonpool gap (Tan et al., 2021). Comparable gap-resonance behavior, driven by vortex shedding at the sharp hull edge adjacent to a rigid boundary, has also been shown experimentally and numerically to produce strong nonlinear damping of the confined fluid response (Milne et al., 2022).

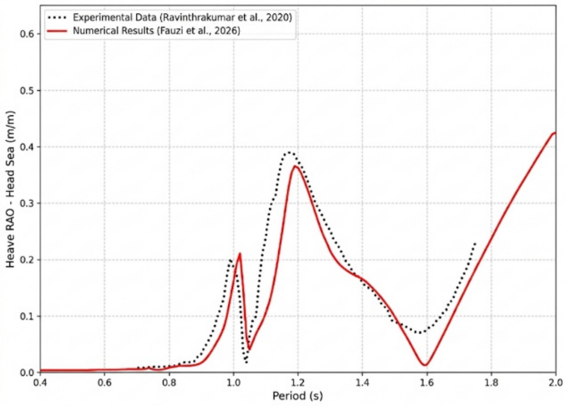

Figure 1. Heave response comparison with a moonpool

Note. Adapted from "Hydrodynamic Responses of Floating Oscillating Water Column for Wave Energy Conversion," by F. N. Fauzi, D. Satrio, and R. Adiputra, 2026, *E3S Web of Conferences*, 687, Article 01010 (https://doi.org/10.1051/e3sconf/202668701010). Experimental data adapted from "Coupled Vessel and Moonpool Responses in Regular and Irregular Waves," by S. Ravinthrakumar, T. Kristiansen, B. Molin, and B. Ommani, 2020, *Applied Ocean Research*, 96, Article 102010 (https://doi.org/10.1016/j.apor.2019.102010).

The most important fluid-dynamics challenge to anticipate, aside from drag, is piston-mode resonance. As foundational studies have shown, wave-induced water motion inside a moonpool primarily occurs at its natural modes, specifically the sloshing modes (where water oscillates back and forth between walls) and the piston mode, where the enclosed water column heaves vertically, acting somewhat like a rigid body (Molin, 2001). Unlike closed tanks, the open bottom of the moonpool allows a nonzero mass flux, which is the primary driver of this piston-mode manifestation (Molin, 2001). A structure will experience critical oscillatory resonance when the frequency of the incident wave approaches the natural frequency of the fluid inside the moonpool tube (Yang et al., 2013; Guo et al., 2017). As a result of this phenomenon, the entire ship body experiences a sharp increase in vertical translational motion, or heave (Jiang et al., 2023; Kristiansen & Faltinsen, 2010), as clearly illustrated in Figure 1. Accurately predicting this surge is computationally complex; a study of a three-dimensional cylindrical moonpool has shown that vortex-shedding-induced viscous effects measurably alter the free-surface elevation and hydrodynamic coefficients near resonance effects that an inviscid boundary-element formulation alone cannot capture (Han et al., 2024). Consequently, to mitigate these severe resonant motions in physical applications, tests have demonstrated that piston-mode amplification can be substantially suppressed through dedicated damping devices such as flap grids and baffle arrays (Huang et al., 2020).

Due to their much higher computational efficiency than Computational Fluid Dynamics (CFD) methods, traditional numerical techniques based on the Boundary Element Method (BEM) have become the industry standard for predicting these complex motion anomalies (Siddiqui et al., 2023). Recent cross-validation studies have further confirmed that panel-based BEM solvers such as ANSYS AQWA reproduce frequency-domain hydrodynamic coefficients and motion RAOs within close agreement of independent potential-flow codes, reinforcing their continued use as a reliable first-pass design tool (Park et al., 2025). To analyze the sensitivity of the ship motion response, numerical evaluation of changes in the hull size ratio and opening configuration has proven crucial (Fauzi et al., 2026). Experimental investigations of vessels incorporating multiple moonpools have further revealed that resonant free-surface responses and their phase relationships differ substantially between forward, central, and aft openings, with the coupling between moonpool oscillation and the vessel's own heave and pitch motions producing distinct, location-dependent resonance peaks (Garad et al., 2024). This study addresses the following research questions: (1) How accurately can the Boundary Element Method (BEM), as implemented in ANSYS AQWA, replicate the Heave RAO curve of a multi-moonpool floating structure under head-sea wave conditions? (2) How sensitive is the predicted RAO to mesh resolution, based on a systematic grid independence study? (3) To what extent do the theoretical limitations of BEM affect its ability to represent fluid resonance within the moonpool openings?

■ METHOD

Mathematical Formulation of Wave and Floating Structure Interaction

The hydrodynamic modeling in this study is based on Potential Flow Theory. This mathematical approach assumes that the fluid (seawater) is inviscid, incompressible, and irrotational (Siddiqui et al., 2023). This classical linearized potential-flow formulation has historically proven highly effective in treating both two- and three-dimensional moonpool oscillation problems under the assumption of infinite water depth (Molin, 2001). Based on these assumptions, the scalar flow velocity potential, Φ(x,y,z,t), is conditioned to satisfy the law of conservation of mass through the Laplace Equation within the fluid domain:

$$\nabla^2 \Phi = 0 \qquad (1)$$

The solution to the Laplace Equation requires the establishment of boundary conditions across the entire computational domain (Fauzi et al., 2026):

Seabed boundary condition: Assumes no fluid flow penetrates the seabed at depth *z=-d*,

$$\frac{\partial \Phi}{\partial z} = 0 \qquad (2)$$

Free surface boundary condition: A linear combination of kinematic and dynamic conditions at the undisturbed water surface elevation *(z=0)*,

$$\frac{\partial \Phi}{\partial z} = -\frac{1}{g}\frac{\partial^2 \Phi}{\partial t^2} \qquad (3)$$

Body surface boundary condition: The velocity of the fluid particles directly in contact with the structure's hull must equal the normal velocity of the body element (v_n),

$$\frac{\partial \Phi}{\partial n} = v_n \qquad (4)$$

The total flow potential is the sum of the incident wave, diffraction, and radiation potentials. The hydrodynamic pressure (*p*) is obtained through the linearized Bernoulli Equation:

$$p = -\rho \frac{\partial \Phi}{\partial t} - \rho g z \qquad (5)$$

The area integration of the fluid pressure across the immersed hull webs (including the internal curvature planes of the seven moonpool tubes) is translated into an added mass matrix (A_{jk}) and a wave radiation attenuation (B_{jk}) (Fauzi et al., 2026). The 6-DOF matrix Newtonian equation of motion is expressed as:

$$\Sigma_{j,k=1}^{6}\left[-\omega^2\left(M_{jk} + A_{jk}(\omega)\right) + i\omega B_{jk}(\omega) + C_{jk}\right]\xi_k = F_j(\omega) \qquad (6)$$

In the formulation of equation (6) above, ω indicates the circular frequency of the wave, M_{jk} is the mass inertia matrix of the structure, C_{jk} represents the hydrostatic restoring force of the water plane, ξ_k is the amplitude response displacement, and F_j is the combined Froude-Krylov excitation force. The analysis in this study is focused on solving the vertical motion amplitude parameters (xi_3)expressed in the form of a non-dimensional Response Amplitude Operator (RAO) Heave (Fauzi et al., 2026).

Multi-Moonpool Architectural Design and Floating Structure Geometry

This study models the object using a full-scale displacement-type architecture. To ensure reproducibility of the hydrodynamic simulations, the geometric configuration focuses exclusively on this specific monohull design. As shown in Figure 2, the structural configuration comprises a primary moonpool unit located amidships, accompanied by several additional cylindrical openings distributed sequentially along the hull's longitudinal axis.

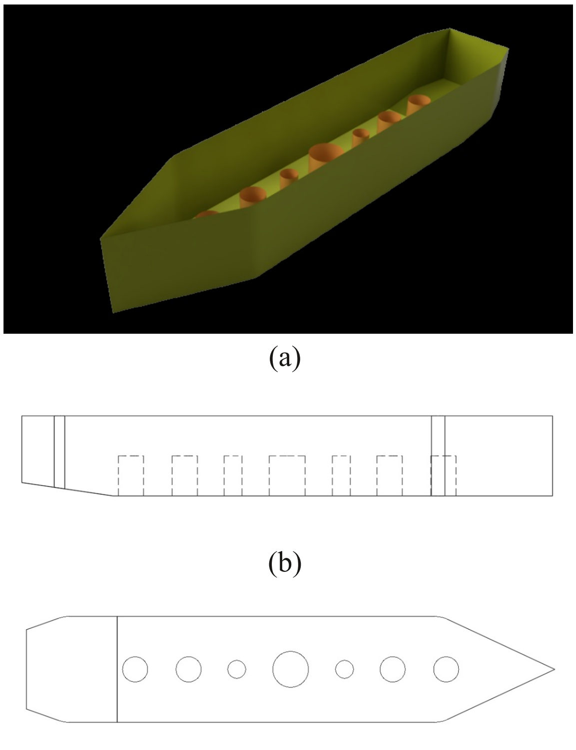

(a) (b) (c)

Figure 2. Ship geometry with multi-moonpool configuration: (a) isometric, (b) plan, and (c) profile views.

Note. Model generated in the surface (shell) CAD environment prior to import into ANSYS AQWA. Panel (a) shows the isometric view of the full hull with the main moonpool and additional moonpool groups. Panels (b) and (c) show the plan and profile views. These verify moonpool spacing and longitudinal placement relative to the aft perpendicular (AP).

Specific parameters of the multi-moonpool system, including the diameter, number, and center-to-center spacing of consecutive openings, are defined to enable accurate replication of the displaced buoyancy volume and fluid resonance conditions. Comprehensive dimensional specifications for both the main hull and the integrated moonpool system are showed in Table 1.

Table 1. Principal dimensions of the hull and multi-moonpool system.

Parameters	Variable	Value	Units
Length Overall	LoA	177.300	meter
Beam	B	35.464	meter
Draft	d	13.299	meter
Main Moonpool			
Diameter	D_{main}	11.89	meter
Location of Main Moonpool (from AP)	L_{main}	88.66	meter
Additional Moonpool A			
Diameter	$D_{add,A}$	8.44	meter
Quantity	N_A	4	units
Center-to-Center Spacing	$S_{cc,A}$	17.97	meter
Additional Moonpool A			
Diameter	$D_{add,B}$	5.99	meter
Quantity	N_B	2	units
Center-to-Center Spacing	$S_{cc,B}$	18.09	meter

Note. LoA = length overall; B = beam; d = draft; D = moonpool diameter; L = longitudinal location of the moonpool centerline measured from the aft perpendicular (AP); S = center-to-center spacing between adjacent moonpool openings; N = number of moonpool units per group. Subscript main denotes the main moonpool. Subscripts add,A and add,B denote the two additional moonpool groups, A and B, respectively. All dimensions are full-scale values used directly as CAD input for the ANSYS AQWA diffraction model.

Inertia Matrix Equivalence and Weight Parameters

A major challenge in dynamic computation is determining the center of inertia for a hull with multiple large openings, since each cylindrical moonpool locally removes buoyant volume and shifts the mass distribution away from a simple prismatic hull assumption. To resolve this, the radii of gyration (K_{xx}, K_{yy}, K_{zz}) were extracted directly from the mass-properties check of the three-dimensional surface (shell) CAD model, which explicitly accounts for the volume removed by the main moonpool and the sequential cylindrical openings.

Since the model represents the outer hull envelope rather than a full solid model with internal structural detail (decks, bulkheads, and equipment), an equivalent uniform mass distribution over the enclosed hull volume was assumed to represent the combined effect of structural steel and operational payload. These CAD-derived inertia values, together with the assigned center of gravity, were then cross-verified using the Hydrostatics module in ANSYS AQWA to confirm consistency between the computed metacentric height, buoyancy, and the target displacement before proceeding to the diffraction analysis. The finalized mass and inertia properties applied to stabilize the solver's calculation matrix are detailed in Table 2.

Table 2. Mass properties and inertia parameters.

Parameters	Variable	Value	Units
Total Displacement Mass	M	68,205.7	MT
Roll Radius of Gyration	K_{xx}	12.05	meter
Pitch Radius of Gyration	K_{yy}	44.33	meter
Yaw Radius of Gyration	K_{ZZ}	46.10	meter
Longitudinal Center of Gravity	LCG	-6.77	meter
Vertical Center of Gravity	VCG	2.90	meter

Note. M = total displacement mass; MT = metric tons. Radii of gyration and center-of-gravity values were extracted from the mass-properties check of the three-dimensional shell CAD model. The check accounts for the buoyant volume removed by the main and additional moonpool openings. These values were cross-verified against the Hydrostatics module in ANSYS AQWA prior to the diffraction analysis.

Marine Domain Restriction and Simulation Environment

To obtain a pure wave propagation profile free from seabed reflection interference, simulations were conducted assuming infinite water depth with the wave direction fixed at 180° (head sea). To capture the hydrodynamic response comprehensively, the simulations encompassed a spectrum spanning both high-frequency piston-mode resonance and the lower-frequency macro-wave regime. The specific wave periods and frequency ranges used in the diffraction analysis are summarized in Table 3. The selected frequency range ensures that the piston-mode resonance peak is fully captured, along with the vessel's rigid-body motion characteristics.

Table 3. Simulation parameters for wave frequency and period.

Parameters	Range/Value	Units
Wave Period Range	1.84 to 62.83	second (s)
Wave Frequency Range	0.10 to 3.41	rad/s
Wave Heading	180	degrees (°)
Water Depth	Infinite	-

Note. Wave frequency and period values define the range of incident regular waves applied under head-sea (180-degree) conditions in the ANSYS AQWA diffraction-radiation solver, using linearized potential-flow theory.

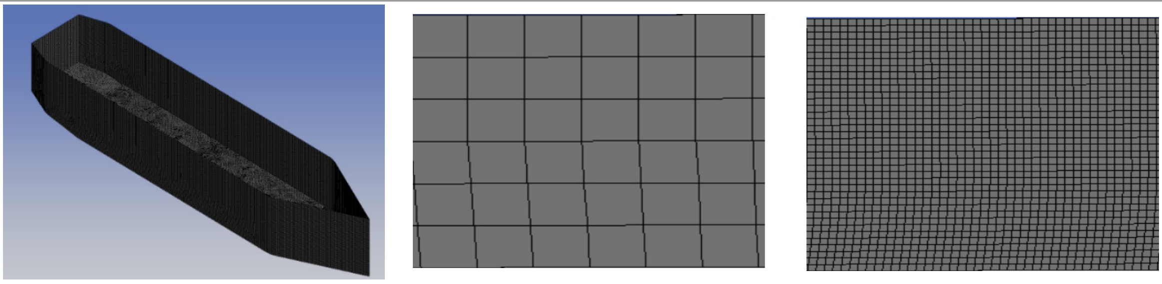

Figure 3. Computational mesh of the ship model: (a) isometric view, (b) 0,7m mesh detail, and (c) 5m mesh detail.

Note. Diffraction-radiation panel mesh generated in ANSYS AQWA using a full-body model (no longitudinal symmetry) covering the complete wetted hull and internal moonpool surfaces. Panel (a) shows the isometric view of the meshed hull and moonpool surfaces. Panels (b) and (c) show close-up views of the 0.7 m (final, selected) and 5.0 m (coarsest) panel resolutions, respectively. This illustrates the refinement applied near the intersection of the moonpool free surface.

BEM Convergence and Mesh Discretization

This study employs the Boundary Element Method (BEM), implemented in ANSYS AQWA, to evaluate the hydrodynamic response of a new monohull prototype. To ensure computational accuracy and to eliminate numerical errors associated with spatial discretization, a systematic grid-independence test was conducted. The hull structure, including the internal curvature of the moonpool, was discretized using a combination of triangular and quadrilateral panels. The grid-independence study evaluated mesh adequacy and yielded a relative difference of 0.50% at the first resonance peak. Mesh resolution was systematically varied, ranging from a coarse grid size of 5.0 m to a fine grid size of 0.7 m. Visual representations of the computational mesh at various levels of refinement are shown in Figure 3.

The refinement process evaluated the convergence behavior at the critical frequencies, specifically observing the stability of the first and second resonance peaks. The detailed evaluation of the number of elements and the corresponding relative difference in peak amplitudes is summarized in Table 4.

As depicted in the asymptotic distribution curve in Figure 4, the response amplitude stabilizes and reaches a plateau as the mesh density increases. The optimal mesh resolution of 0.7 m, which generated 38,748 elements, was adopted for the final operational simulation. At this size, the relative difference percentage at the first peak reached 0.50%, confirming absolute grid convergence well below the conventional numerical tolerance limit. This criterion is consistent with mesh-independence practices reported in comparable ANSYS AQWA-based potential-flow validation studies, in which relative differences of less than 1% between successive mesh refinements are used as the benchmark for a converged, panel-count-limited hydrodynamic solution (Qu & Yao, 2022). As observed in the data, the non-monotonic trend at coarser resolutions (5.0-1.5 m) reflects the sensitivity of panel-based discretization to the sharp pressure gradients near the moonpool free-surface intersection at piston-mode resonance. Small changes in panel arrangement between successive mesh densities alter how the localized resonant peak is

Table 4. Mesh convergence evaluation based on the number of elements and the relative difference of peak amplitudes.

Mesh Resolution (m)	Total Elements	1st Peak RAO (m/m)	Relative Dif 1 (%)	2nd Peak RAO (m/m)	Relative Dif 2 (%)
5.0	954	0.21974	-	0.99901	-
4.0	1,523	0.23273	5.91	0.99907	0.006
3.0	2,487	0.22404	3.73	0.99907	0.000
2.0	5,158	0.24542	9.54	0.99910	0.003
1.5	8,775	0.26735	8.94	0.99910	0.000
1.0	19,636	0.27102	1.37	0.99910	0.000
0.7	38,748	0.26966	0.50	0.99911	0.001

Note. Relative Dif 1 (%) and Relative Dif 2 (%) denote the percentage change in the 1st and 2nd peak Heave RAO values between successive mesh resolutions, computed as $|(RAO_n - RAO_{n-1})/RAO_{n-1}| \times 100$, where RAO_n is the peak value at the current mesh resolution, and RAO_{n-1} is the value at the next coarser resolution. RAO = Response Amplitude Operator.

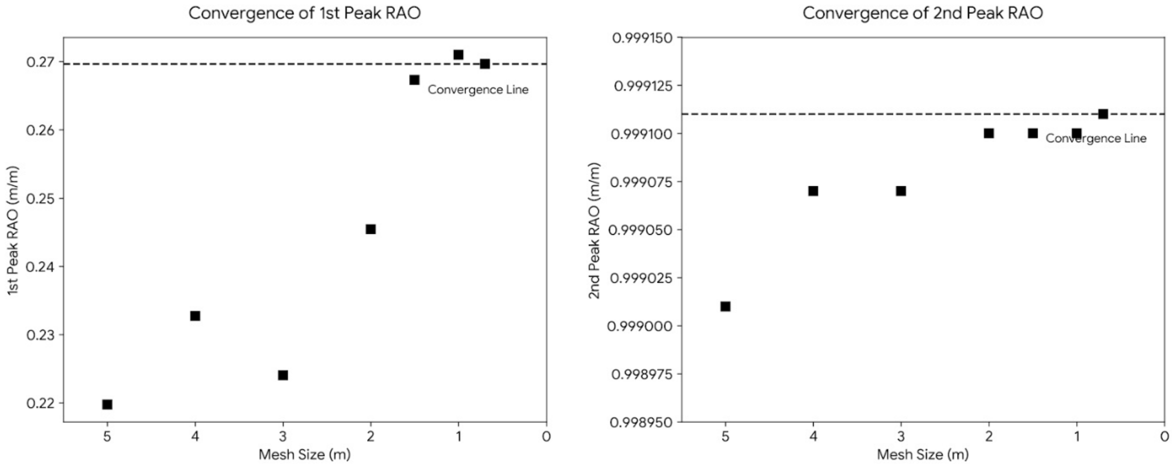

Figure 4. Asymptotic distribution curve of mesh convergence at the first and second resonance peaks.
Note. Convergence of the 1st (piston-mode) and 2nd (macro-wave) peak Heave RAO values against mesh element size, corresponding to the mesh resolutions and relative differences reported in Table 4.

resolved before the solution enters the stable asymptotic convergence regime beyond 1.5 m. This behavior contrasts with the 2nd Peak RAO (macro-wave regime), which converges monotonically because it is governed by smoother, less singular flow features.

Basis for Cross-Validation with Reference Geometry

To directly address the validity of the Heave RAO cross-validation presented in Figure 5, Table 5 compares the principal hull and moonpool parameters of the present study with those of Geometry 1. The Geometry 1 hull parameters and reference Heave RAO data were obtained directly from the corresponding author through personal communication. The data were provided by the author and were not digitized, estimated, or reconstructed from published sources.

As summarized in Table 5, the present study and Geometry 1 share identical principal hull geometry and moonpool configuration. The length overall, beam, and draft are identical. Both hulls feature the same number and sequential arrangement of moonpool openings. The displacement mass differs by approximately 0.075% (68,205.700 MT for the present study and 68,256.891 MT for Geometry 1). This difference is reported for transparency. They were not digitized, estimated, or reconstructed from published sources. On this basis, Figure 5 compares the non-dimensional Heave RAO (ξ_3/ζ_a) as a function of wave period.

■ RESULTS AND DISCUSSION

With the operating mesh resolution established through the grid-independence study described in the Method section (Table 4,

Table 5. Comparison of principal hull and moonpool parameters between the present study and geometry 1.

Parameter	Present Study (Current)	Geometry 1 (Reference)
Scale	Full-scale	Full-scale
Length Overall, LOA (m)	177.30	177.30
Beam, B (m)	35.464	35.464
Draft, T (m)	13.299	13.299
Number of Moonpools	7 (1 main + 6 additional)	7 (1 main + 6 additional)
Moonpool Configuration	Sequential, multiple diameters	Sequential, multiple diameters
Displacement Mass (MT)	68,205.700	68,256.891
Relative Displacement Difference (%)	-	≈ 0.075%
Comparison Basis	Non-dimensional Heave RAO (ξ3/ζa) vs. wave period	Non-dimensional Heave RAO (ξ3/ζa) vs. wave period

Note. Geometry 1 = independent reference hull and moonpool geometry used for Heave RAO cross-validation. Geometry 1 hull parameters and reference Heave RAO data were obtained directly from the corresponding author of the reference study through personal communication. The data were not digitized, estimated, or reconstructed from published sources.

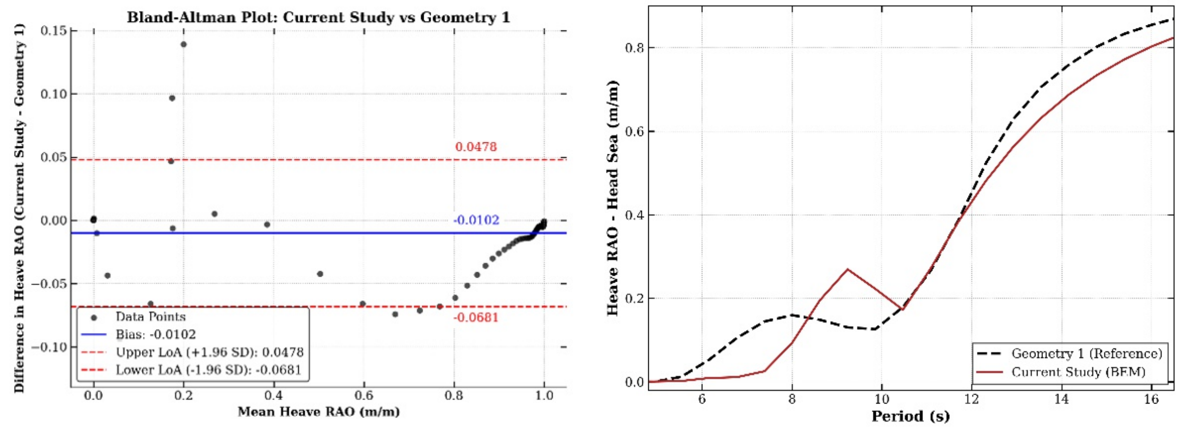

Figure 5. Comparison of Heave RAO Profiles between Present BEM Study and Reference Data under Head Sea Condition: (a) Heave RAO comparison and (b) Bland-Altman analysis.

Note. Panel (a) overlays the non-dimensional Heave RAO (Current Study, BEM) against the Geometry 1 reference curve across the tested wave-period range. Panel (b) is a Bland-Altman plot of the paired Heave RAO differences (Current Study - Geometry 1) against their mean, with the solid line indicating the bias and the dashed lines indicating the 95% limits of agreement (bias +/- 1.96 SD). Geometry 1 reference data source as described in the note to Table 5

Figure 4), the resulting Heave RAO curve was benchmarked against reference data to evaluate the hydrodynamic performance of the multi-moonpool structure.

Based on this analysis, the 0.7 m element size was adopted as the final operational resolution. At this size, the relative difference percentage at the 1st Peak reached 0.50%, well below the conventional numerical tolerance limit (2%), confirming the occurrence of absolute grid convergence with a total of 38,748 elements. The benchmarking process compared the BEM-computed Heave RAO profile (Current Study) directly with the Geometry 1 reference curve. This comparison under head-sea excitation is presented in Figure 5, which now comprises two panels: (a) the Heave RAO overlay, and (b) a Bland-Altman analysis of the paired dataset. Geometry 1 shares the same principal hull and moonpool parameters as the present study, as summarized in Table 5. The reference dataset serves as the validity checkpoint for the BEM matrix distribution pattern.

a. (b)

Figure 5(a) divides the hydrodynamic behavior into two regions. In the macro-wave regime, the BEM curve closely tracks Geometry 1. Near the moonpool resonance peak, a pronounced amplitude gap appears. Geometry 1 reaches its resonance peak at a wave period of 8.00 s, with a peak Heave RAO of 0.1598. The Current Study reaches its peak at 9.24 s, with a peak Heave RAO of 0.2697. This corresponds to a 1.24 s phase shift. The BEM solver overpredicted the peak amplitude by 68.77% relative to the peak.

This overprediction is consistent with the known limitations of inviscid potential-flow solvers. Such solvers neglect viscous dissipation. They also neglect flow-separation effects near moonpool resonance (Fu et al., 2026). Dedicated viscous-damping corrections applied to recessed moonpool models have brought boundary-element predictions closer to nonlinear numerical results (Chu et al., 2022). This correction pathway remains promising for refining the present BEM formulation.

Radiation damping from CFD simulations of a floating wind turbine hull was found to exceed potential-flow predictions (Siddiqui et al., 2023). This gap was attributed to viscous flow effects. Comparable resonance-driven amplification has been reported for a moonpool-equipped drillship hull under combined CFD and physical-model analysis, where the free-surface elevation inside the moonpool reached over twice the incident wave height once the encountered wave frequency coincided with the moonpool's natural frequency (Guo et al., 2017). A related drag-reduction study on moonpool drillships in irregular waves attributes near-resonance behavior to viscous and vortex-shedding effects (Hu et al., 2026). Inviscid BEM formulations cannot resolve such effects.

Kristiansen and Faltinsen reported that linear potential-flow theory overpredicted piston-mode amplitudes near resonance by approximately 240-300% for a freely moving ship section (Kristiansen & Faltinsen, 2010). The overprediction fell to 45-65% for the simpler forced-motion radiation problem. Their configuration used sway-restoring mooring springs. The heave- and roll-restoring forces remained purely hydrodynamic. This makes the comparison indicative rather than directly equivalent to the present linear BEM model in ANSYS AQWA. It nevertheless offers a useful benchmark for the magnitude of resonance overprediction in inviscid potential-flow formulations.

The 68.77% relative peak difference presented in Table 6 lies well below the highest overprediction levels reported previously (Kristiansen & Faltinsen, 2010). This result is consistent with the expected behavior of linear potential-flow solvers that lack viscous damping or flow-separation corrections. A comparable magnitude of resonance overprediction has been reported for coupled moonpool-hull systems under mooring restraint (Jiang et al., 2024). There, inviscid potential-flow solvers similarly amplified the piston-mode peak relative to viscous CFD benchmarks. This indicates that the limitation persists across different hull and mooring configurations.

Direct quantitative comparison should still be interpreted with caution. Resonance amplitudes are strongly influenced by moonpool geometry, degrees of freedom, boundary conditions, and mooring configuration.

To quantify agreement between the two datasets across the full wave-period range, a Bland-Altman analysis was performed, following the original method (Bland & Altman, 1986). Figure 5(b) plots the difference between paired Heave RAO values against their mean, for n = 100 paired observations. The analysis yields a bias of -0.01016. The standard deviation of the differences is 0.02958. The 95% limits of agreement span from -0.06813 to 0.04781. The maximum absolute difference across all pairs is 0.13908, while the mean absolute difference is 0.01323.

Most data points, corresponding to the macro-wave regime, fall within the 95% limits of agreement. This distribution supports the reliability of the BEM solver away from resonance. The near-zero bias further indicates no systematic offset over most of the wave-period range. The points exceeding the limits of agreement correspond directly to the high-frequency piston-mode resonance zone. This pattern is consistent with the absence of viscous damping in the BEM formulation. It confirms that the disagreement between the two datasets is localized, rather than distributed across the full response curve.

Taken together, the low mean absolute difference (0.01323) against the substantially higher maximum absolute difference (0.13908) reinforces this localization. The bulk of the paired dataset agrees closely. A small subset of points, concentrated at resonance, drives the wider spread. This magnitude of overprediction is consistent with an independent AQWA-based validation of a floating oscillating water column device. There, inviscid potential-flow predictions of heave and pitch RAO near the moonpool resonance period exceeded experimental measurements by approximately 48-52%, with the discrepancy vanishing away from resonance (Pols et al., 2021).

Emerging two-way coupled potential-viscous flow frameworks couple a fully nonlinear potential-flow solver for the far-field wave domain with a localized Navier-Stokes solver near the structure. These frameworks have accurately reproduced wave-induced loads while sharply reducing computational cost relative to full CFD (Landesman et al., 2024). Such frameworks offer a promising route toward correcting this class of BEM overprediction in future multi-moonpool design studies. A Bland-Altman-style agreement analysis, as applied here, offers a complementary statistical lens for quantifying this bias beyond a single peak-difference metric.

It is important to note that these conclusions are confined to the vessel's motion response. No structural stress or strength analysis was performed in this study. The findings should not be interpreted as a general assessment of hull structural integrity. These results indicate that BEM remains a computationally efficient and reliable tool for early-stage seakeeping assessment of multi-moonpool floating structures away from resonance. Resonance-sensitive design decisions require a viscous damping correction. Future work should focus on developing and experimentally validating such damping

Table 6. Comparison of heave rao peak values at piston-mode resonance.

Parameter	Geometry 1 (Reference)	Current Study (BEM)	Deviation
Resonance Wave Period (s)	8.00	9.24	+ 1.24 s
Peak Heave RAO (m/m)	0.1598	0.2697	+ 68.77%

Note. Relative Peak Difference (%) for Peak Heave RAO = [(RAOCurrent Study - RAOGeometry 1) / RAOGeometry 1] x 100. Positive values indicate overprediction by the present BEM (boundary element method) benchmark relative to Geometry 1. Reference data source as described in the note to Table 5.

modifiers. Promising avenues include model-scale testing, coupled CFD-BEM approaches, and emerging two-way coupled potential-viscous flow frameworks. These approaches would improve the accuracy of moonpool resonance predictions. They would also support more robust hydrodynamic optimization of next-generation floating structures.

■ CONCLUSIONS

This study demonstrated the applicability of the Boundary Element Method (BEM), implemented in ANSYS AQWA, for evaluating the hydrodynamic motion response of a full-scale displacement-type floating structure with a multi-moonpool configuration under head-sea conditions. The grid independence study showed different convergence characteristics across the investigated response regimes. The macro-wave regime exhibited a relatively smooth convergence pattern. The piston-mode resonance region showed non-monotonic convergence at coarser mesh resolutions. This behavior reflects the sensitivity of panel-based discretization to the localized hydrodynamic response around the moonpool. A mesh resolution of 0.7 m was selected as the final operational mesh. This resolution comprised 38,748 elements and yielded a relative difference of 0.50% at the first peak. The result satisfied the adopted numerical tolerance of 2%.

Benchmarking against Geometry 1 showed that the BEM model reproduced the Heave RAO profile satisfactorily in the macro-wave regime. The difference between the two datasets remained relatively small across this region. The Bland-Altman analysis also indicated good agreement across most paired observations. The calculated bias was -0.01016. The mean absolute difference was 0.01323. The largest differences were concentrated around the piston-mode resonance region. This finding indicates that the disagreement was localized rather than distributed across the investigated wave-period range.

A significant discrepancy was observed at piston-mode resonance. Geometry 1 reached a peak Heave RAO of 0.1598 m/m at a wave period of 8.00 s. The present BEM model predicted a peak of 0.2697 m/m at 9.24 s. The resulting resonance-period shift was 1.24 s. The peak Heave RAO was overpredicted by 68.77%. This discrepancy is primarily associated with the inviscid formulation of the BEM approach. The formulation does not explicitly represent viscous dissipation, flow separation, or vortex shedding around the moonpool edges. These effects become more significant near piston-mode resonance. The resulting lack of viscous damping can lead to excessive resonance amplification.

The findings indicate that BEM remains a computationally efficient tool for early-stage seakeeping assessment of multi-moonpool floating structures. Its quantitative accuracy is satisfactory away from resonance. Additional damping treatment is required for resonance-sensitive applications. The present results are limited to hydrodynamic motion response. No structural stress or strength analysis was performed. Therefore, the findings do not constitute an assessment of the hull's structural integrity.

Future studies should focus on improving resonance prediction through viscous-damping corrections. Model-scale experiments can provide experimental validation of the proposed corrections. Coupled CFD-BEM simulations can further resolve viscous effects around the moonpool. Two-way coupled potential-viscous flow frameworks also provide a promising approach. These methods can improve moonpool resonance prediction. They can also support more reliable hydrodynamic optimization of next-generation multi-moonpool floating structures.

■ REFERENCES

Bland, J. M., & Altman, D. G. (1986). Statistical methods for assessing agreement between two methods of clinical measurement. The Lancet, 327(8476), 307–310. https://doi.org/10.1016/S0140-6736(86)90837-8

Chen, M., Yang, L., Sun, X., Pan, J., Zhang, K., Lin, L., Yun, Q., & Chen, Z. (2024). Dynamic Analysis of a Barge-Type Floating Wind Turbine Subjected to Failure of the Mooring System. *Journal of Marine Science and Engineering*, *12*(4). https://doi.org/10.3390/jmse12040617

Chu, B., Zhang, X., & Zhang, Y. (2022). Effects of nonlinearity and viscous damping on the resonant responses in two-dimensional moonpools with a recess. *Applied Ocean Research*, *127*. https://doi.org/10.1016/j.apor.2022.103295

Cui, J., Chen, X., Sun, P. N., & Li, M. Y. (2022). Numerical investigation on the hydrodynamic behavior of a floating breakwater with moon pool through a coupling SPH model. *Ocean Engineering*, *248*. https://doi.org/10.1016/j.oceaneng.2022.110849

Fauzi, F. N., Satrio, D., & Adiputra, R. (2026). Hydrodynamic Responses of Floating Oscillating Water Column for Wave

Energy Conversion. *E3S Web of Conferences*, *687*, 01010. https://doi.org/10.1051/e3sconf/202668701010

Fu, S., Gao, W., Li, Y., Xie, Y., Wang, T., & An, C. (2026). Research on Prediction Method for Heave Motion of Cylindrical FPSO Based on Viscous Correction. *Journal of Marine Science and Engineering*, *14*(5). https://doi.org/10.3390/jmse14050474

Garad, S., Kumar, S., Bhattacharyya, A., & Datta, R. (2024). Multiple moonpools within a vessel free to heave and pitch: An experimental study. *Applied Ocean Research*, *147*. https://doi.org/10.1016/j.apor.2024.103963

Guo, X., Lu, H., Yang, J., & Peng, T. (2017). Resonant water motions within a recessing type moonpool in a drilling vessel. *Ocean Engineering*, *129*, 228–239. https://doi.org/10.1016/j.oceaneng.2016.11.030

Han, J., Zhang, X., Chen, J., & Li, Z. (2024). On coupled hydrodynamic responses of three-dimensional cylindrical moonpools. *Ocean Engineering*, *294*. https://doi.org/10.1016/j.oceaneng.2024.116769

Hu, J., Zhang, Z., Song, C., Wang, J., Yu, X., & Zhang, D. (2026). Motion Characteristics and Drag-Reduction Optimization of Moonpool Drillships in Irregular Waves. *Journal of Marine Science and Engineering*, *14*(10). https://doi.org/10.3390/jmse14100890

Huang, X. H., Xiao, W., Yao, X. L., Gu, J. Y., & Jiang, Z. Y. (2020). An experimental investigation of reduction effect of damping devices in the rectangular moonpool. *Ocean Engineering*, *196*. https://doi.org/10.1016/j.oceaneng.2019.106767

Jiang, S.-C., Lan, J.-J., Bai, W., & Huang, Y.-Q. (2024). Coupling analysis between wave resonance in the moonpool and heave motion of the twin hulls with mooring effect. Physics of Fluids, 36(11), 117118. https://doi.org/10.1063/5.0231467

Jiang, S. C., Ran, Y. Q., & Feng, A. (2023). On the hydrodynamic behaviour of second-order harmonic induced sloshing-mode resonance in moonpool. *Marine Structures*, *92*. https://doi.org/10.1016/j.marstruc.2023.103503

Kristiansen, T., & Faltinsen, O. M. (2010). A two-dimensional numerical and experimental study of resonant coupled ship and piston-mode motion. *Applied Ocean Research*, *32*(2), 158–176. https://doi.org/10.1016/j.apor.2009.10.001

Landesman, P., Harris, J. C., Peyrard, C., & Benoit, M. (2024). Wave–structure interaction by a two–way coupling between a fully nonlinear potential flow model and a Navier–Stokes solver. *Ocean Engineering*, *308*. https://doi.org/10.1016/j.oceaneng.2024.118209

Milne, I. A., Kimmoun, O., Graham, J. M. R., & Molin, B. (2022). An experimental and numerical study of the resonant flow between a hull and a wall. Journal of Fluid Mechanics, 930, Article A25. https://doi.org/10.1017/jfm.2021.877

Molin, B. (2001). On the piston and sloshing modes in moonpools. Journal of Fluid Mechanics, 430, 27–50. https://doi.org/10.1017/S0022112000002871

Park, S. H., Cheon, S. G., & Chung, W. C. (2025). Numerical Analysis Comparison Between ANSYS AQWA and OrcaFlex for a Hollow Box-Shaped Floating Structure. *Journal of Marine Science and Engineering*, *13*(12). https://doi.org/10.3390/jmse13122407

Pols, A., Gubesch, E., Abdussamie, N., Penesis, I., & Chin, C. (2021). Mooring analysis of a floating owc wave energy converter. *Journal of Marine Science and Engineering*, *9*(2), 1–22. https://doi.org/10.3390/jmse9020228

Qu, X., & Yao, Y. (2022). Numerical and Experimental Study of Hydrodynamic Response for a Novel Buoyancy-Distributed Floating Foundation Based on the Potential Theory. *Journal of Marine Science and Engineering*, *10*(2). https://doi.org/10.3390/jmse10020292

Ravinthrakumar, S., Kristiansen, T., Molin, B., & Ommani, B. (2020). Coupled vessel and moonpool responses in regular and irregular waves. *Applied Ocean Research*, *96*. https://doi.org/10.1016/j.apor.2019.102010

Shahabadi, M., shadlaghani, A., & Mansoorzadeh, S. (2017). Evaluation of Moonpool Effects on Hydrodynamic Resistance of a Supply Vessel, Using Experimental and Numerical Methods. *International Journal of Maritime Technology*, *7*, 1–9. https://doi.org/10.18869/acadpub.ijmt.7.1

Sheng, W., Tapoglou, E., Ma, X., Taylor, C. J., Dorrell, R. M., Parsons, D. R., & Aggidis, G. (2022). Hydrodynamic studies of floating structures: Comparison of wave-structure interaction modelling. *Ocean Engineering*, *249*. https://doi.org/10.1016/j.oceaneng.2022.110878

Siddiqui, M. A., Hanssen, F. C. W., Greco, M., & Anda, E. (2023). Comparing the Utility of Coupled Aero-Hydrodynamic Analysis

Using a CFD Solver versus a Potential Flow Solver for Floating Offshore Wind Turbines. *Energies*, *16*(23). https://doi.org/10.3390/en16237833

Sulovsky, I., Hauteclocque, G. de, Greco, M., & Prpić-Oršić, J. (2023). Comparative Study of Potential Flow and CFD in the Assessment of Seakeeping and Added Resistance of Ships. *Journal of Marine Science and Engineering*, *11*(3). https://doi.org/10.3390/jmse11030641

Tan, L., Ikoma, T., Aida, Y., & Masuda, K. (2021). Mean wave drift forces on a barge-type floating wind turbine platform with moonpools. *Journal of Marine Science and Engineering*, *9*(7). https://doi.org/10.3390/jmse9070709

Yang, S. H., Yang, Y. J., Lee, S. B., Do, J., & Kwon, S. H. (2013). Study on Moonpool Resonance Effect on Motion of Modern Compact Drillship. *Journal of Ocean Engineering and Technology*, *27*(3), 53–60. https://doi.org/10.5574/ksoe.2013.27.3.053

Zhai, H., Yan, C., Shi, W., Zhang, L., Zeng, X., Han, X., & Michailides, C. (2025). Experimental Study on the Hydrodynamic Analysis of a Floating Offshore Wind Turbine Under Focused Wave Conditions. *Energies*, *18*(15). https://doi.org/10.3390/en18154140

Zhao, X., Xue, F., Chen, L., Göteman, M., Han, D., Geng, J., & Sun, S. (2023). Hydrodynamic analysis of a floating platform coupled with an array of oscillating bodies. *Ocean Engineering*, *287*. https://doi.org/10.1016/j.oceaneng.2023.115439

Zou, L., Zhao, Z., Sun, J., Sun, Z., Luo, Z., & Yu, Z. (2024). Numerical analysis of hydrodynamic characteristics in mooring platforms with diverse moonpool shapes using SPH. *Ocean Engineering*, *297*. https://doi.org/10.1016/j.oceaneng.2024.117037